

# Numerical Investigation of Lateral Jets Over Body of Revolution in Supersonic Crossflow

Jun-Mei Zhang\*

National University of Singapore 117576, Republic of Singapore

Y. D. Cui<sup>†</sup> and Jinsheng Cai<sup>†</sup>

National University of Singapore 117411, Republic of Singapore

and

Hua-Shu Dou<sup>‡</sup>

Zhejiang Sci-Tech University, 310018 Hangzhou, People's Republic of China

DOI: 10.2514/1.B34171

In this paper, the flowfield induced by a sonic lateral jet in a supersonic crossflow of Mach number 3.3 around a body of revolution is numerically studied. The numerical simulation is first validated for the case of a circular nozzle. Shock and vortical structures are examined and compared with those of jet in crossflow over a flat plate. It is found that horseshoe vortices are generated from the flow separation region before the jet orifice. They are shed laterally along the footprint of the jet bow shock, wrapping the body of revolution. This wrapping effect is absent in the case of the crossflow over a flat plate. Effects of the jet nozzle shape on the flow structure are further investigated and analyzed. These nozzles, including circular, elliptical, dropletlike, and inverse dropletlike shapes, have equivalent cross-sectional area. The elliptical nozzle with its semimajor axis in the lateral direction has the largest force amplification factor and is thus the most effective. The detailed flow structures also indicate that the low-pressure region aft of the jet is not only closely related with the surface trailing vortices, but also with the indent and reflection lines of the leeward barrel shock.

## Nomenclature

$C_j$	= jet thrust coefficient
$C_m$	= momentum coefficient
$C_n$	= total normal force coefficient
$C_p$	= pressure coefficient
$D$	= diameter of ogival cylinder body, mm
$d$	= reference diameter of jet nozzle, mm
$e$	= major semi-axis of elliptic nozzle, mm
$F$	= normal force, N
$H$	= total enthalpy, J
$h$	= static enthalpy, J
$K$	= jet-interaction amplification factor, $(F_j + F_{ij})/F_j$
$k$	= turbulent kinetic energy, $\text{m}^2/\text{s}^2$
$L$	= length of jet nozzle along the $x$ -coordinate, mm
$l$	= minor semi-axis of elliptic nozzle, mm
$M$	= Mach number
MPR	= momentum parameter ratio, $P_j \gamma_j M_j^2 / P_\infty \gamma_\infty M_\infty^2$
$P$	= static pressure, Pa
$P_t$	= total pressure, Pa
PR	= pressure ratio, PR = $P_{j,t}/P_\infty$
Prt	= turbulent Prandtl number
$T$	= temperature, K
$u_i$	= velocity at the Cartesian coordinate, m/s

Presented as Paper 2009-1477 at the 47th AIAA Aerospace Sciences Meeting Including The New Horizons Forum and Aerospace Exposition, Orlando, FL, 5–8 January 2009; received 3 November 2010; revision received 2 September 2011; accepted for publication 18 September 2011. Copyright © 2011 by the American Institute of Aeronautics and Astronautics, Inc. All rights reserved. Copies of this paper may be made for personal or internal use, on condition that the copier pay the \$10.00 per-copy fee to the Copyright Clearance Center, Inc., 222 Rosewood Drive, Danvers, MA 01923; include the code 0748-4658/12 and \$10.00 in correspondence with the CCC.

\*Research Fellow, Department of Mechanical Engineering, 1 Engineering Drive 2; zhangjunmei@gmail.com (Corresponding Author).

<sup>†</sup>Research Scientist, Temasek Laboratories, 5A Engineering Drive 1.

<sup>‡</sup>Professor, Faculty of Mechanical Engineering and Automation. Associate Fellow AIAA.

$\gamma$	= ratio of specific heats
$\lambda$	= thermal conductivity, W/(m K)
$\mu$	= viscosity, Pa s
$\rho$	= density, kg/m <sup>3</sup>
$\phi$	= circumferential angle, deg
$\omega$	= specific dissipation rate, 1/s

## Subscripts

$ij$	= interaction effect
$j$	= jet effect
$r$	= pressure recovering effect
$s$	= flow separation effect
$v$	= flow vacuum effect
$w$	= wrapping effect
$\infty$	= freestream

## I. Introduction

THE jet in crossflow is relevant to a wide variety of engineering applications, such as plume dispersion, gas turbine combustor cooling, turbofan thrust reverser, and reaction control [1]. Recently, this technique has been successfully applied to flight vehicles for maneuvering and steering, as it provides advantages over conventional control surfaces in reducing response time, simplifying antithermal design, and reducing weight and drag [2]. As a consequence of the strong interaction between the jet and the external flow, the resultant reaction control force includes two parts [3]. The first comes directly from the jet thrust, and the other comes from the changes of pressure distribution over the body due to the complicated interaction between the jet and freestream. This complicated interaction can result in a net force opposite to the jet thrust, known as control reversal, especially at low altitudes, low Mach numbers, and low angles of attack [4]. Therefore, it is of the utmost importance to study how the jet interacts with the incoming freestream and affects the performance of a flight vehicle.

The understanding of jet in crossflow structures was initiated by Morkovin et al. [5], and the Advisory Group for Aerospace Research and Development (AGARD) conference proceedings provide

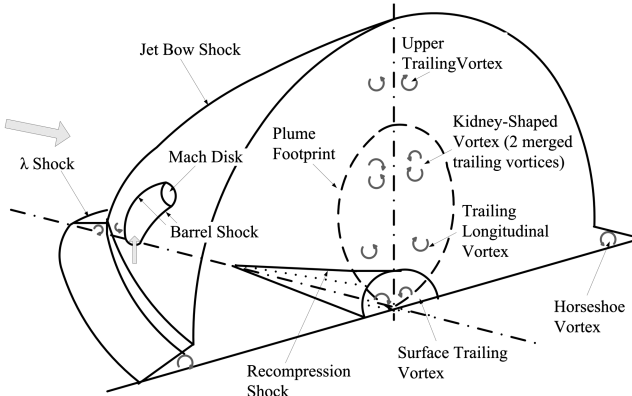


**Fig. 1** Flow structure model for the crossflow over a flat plate (modified from Champigny and Lacau [2] and Viti et al. [8]).

detailed reviews of subsequent work (up to 1994) [1,2]. The widely accepted flow structure model for a jet injecting in the supersonic freestream over a flat plate is summarized by Champigny and Lacau [2] and has been recently elaborated upon by Chenault et al. [6], Lu and Dickmann [7], and Viti et al. [8]. Figure 1 shows the flow structures modified from Champigny and Lacau [2] and Viti et al. [8]. As the jet acts as an obstacle to the external flow, a jet bow shock is generated. The interaction between the jet bow shock and incoming flow boundary layer produces a wedgelike region of separated flow ahead of the jet. In the vicinity of this separation region, a  $\lambda$ -shock, or separation shock, is formed due to the increase of local thickness of the displacement body. After leaving the orifice, the jet expands through a Prandtl-Meyer fan and then recompresses through barrel shocks and ends with a Mach disk. A horseshoe vortex formed ahead of the jet wraps around the upstream side of the jet and trails downstream along the surface. With the downstream movement of the jet plume, complicated wake vortices are formed. Viti et al. [8] identified six primary pairs of vortices downstream of the jet as illustrated in Fig. 1. These are the horseshoe vortices, the upper trailing vortices, two trailing vortices merged as kidney-shaped counter rotation vortices, trailing longitudinal vortices, and the surface trailing vortices [8]. These flow structures greatly affect the flowfield and the pressure distribution over the surface of the flat plate. The flow separation ahead of the jet orifice usually leads to an increase in pressure, whereas a low-pressure region forms aft of the jet injector. This low-pressure region is due to the combined effects of the concave indent in the leeside of the barrel shock and the surface trailing vortices as speculated by Viti et al. [8]. Though an improved description of flow topologies has been achieved from these investigations, they are confined to the crossflow over a flat plate and may be less applicable to the jet in crossflow over a body of revolution.

Studies, such as Champigny and Lacau [2], Brandeis and Gill [3], and Dickmann and Lu [9], have revealed that a body of revolution affects the flowfield of the jet in crossflow and, thus, differs from the crossflow over a flat plate. On one hand, the body bow shock due to the presence of a body of revolution wraps over the body and changes the local pressure of freestream as shown in Fig. 2. On the other hand, the horseshoe vortices, which are formed in the flow separation

region ahead of the jet orifice, shed laterally and move to the bottom part of the body, resulting in unfavorable effects on the jet reaction force. However, detailed knowledge of the flow structures for the jet interaction with a supersonic flow over a body of revolution are still lacking. This motivates us to investigate and identify the differences of a jet in crossflow over a body of revolution with that over a flat plate.

Brandeis and Gill [3] have investigated the effects of geometrical parameters on the crossflow over a body of revolution and found that the forebody shape and length have only a very small influence on the jet-interaction force and the induced pitching moment at supersonic speeds. This has been supported by the numerical study of Graham and Weinacht [10]. Brandeis and Gill [3] also noticed that the force amplification obtained for a cylindrical body is much smaller than that reported by Spaid [11] for two-dimensional (2-D) interactions over a flat plate due to jet wraparound effects. This suggests that the ratio of the jet injection diameter to the body diameter may also affect the interaction because the interaction can be thought of as approximately 2-D if the diameter of the jet injection diameter is much smaller. Furthermore, if the injection nozzle is moved to the aft end of the body, the force amplification factor can be increased due to the elimination of the downstream low-pressure region.

Although a variation in nozzle shape has a significant effect on the flowfield at low-speeds (Haven and Kurosaka [12]), similar studies within the supersonic regime have been less fruitful. Weston and Thamnes [13] reported studies for a circular jet and a rectangular jet (aspect ratio of 4) oriented, respectively, in the streamwise and blunt directions from a flat plate. Greatest penetration into the freestream was found for the streamwise jet and the least for the blunt jet, whereas the circular jet was in between. Barber et al. [14] experimentally evaluated a wedged-shaped and a circular jet orifice on a flat plate. The wedge-shaped injector was found to have no upstream separation zone ahead of the jet, whereas the circular injector had a large separation zone. Gruber et al. [15] investigated sonic transverse injection from circular and elliptic nozzles on a flat plate into a supersonic crossflow with planar Rayleigh/Mie scattering. Although these studies focus on the crossflow over a flat plate at supersonic regime, the detailed effect of nozzle shape on the flow structures and lateral force generation over a body of revolution is limited. This forms the basis for the second objective of this study.

## II. Computational Approach

### A. Governing Equations, Mesh Generations and Boundary Conditions

Although Reynolds-time-averaged Navier-Stokes (RANS) modeling cannot capture detailed time-accurate information, it is capable of capturing the main flow structures [7,16,17]. It is, therefore, employed in this study to investigate the flowfield induced by a lateral jet in crossflow over a body of revolution. The governing equations of a compressible turbulent flow are presented using time-averaged values of density, pressure, velocity components, and temperature as shown in Eqs. (1–4).

The conservation equation of mass is as follows:

$$\frac{\partial \rho}{\partial t} + \frac{\partial(\rho u_i)}{\partial x_i} = 0 \quad (1)$$

The conservation equation of momentum can be computed as

$$\begin{aligned} \frac{\partial}{\partial t}(\rho u_i) + \frac{\partial}{\partial x_i}(\rho u_i u_j) &= -\frac{\partial p}{\partial x_i} + \frac{\partial}{\partial x_i}\left(\mu\left(\frac{\partial u_i}{\partial x_j} + \frac{\partial u_j}{\partial x_i} - \frac{2}{3}\delta_{ij}\frac{\partial u_l}{\partial x_l}\right)\right) \\ &\quad + \frac{\partial}{\partial x_i}(-\rho \bar{u}_i \bar{u}_j) + \rho g_i \end{aligned} \quad (2)$$

The conservation of energy is written as

$$\frac{\partial}{\partial t}(\rho e_0) + \frac{\partial}{\partial x_i}(\rho e_0 u_i + p u_i + \rho \bar{e}_0 \bar{u}_i) = \frac{\partial}{\partial x_i}(\tau_{ij} u_j) - \frac{\partial \bar{q}_i'}{\partial x_i} \quad (3)$$

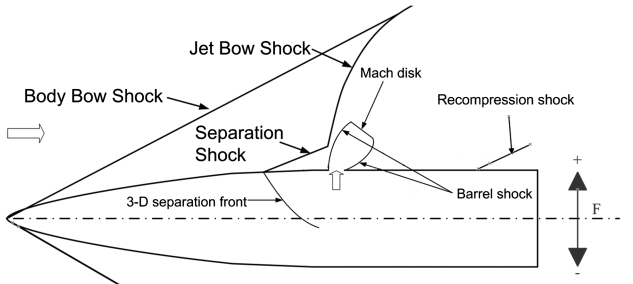


**Fig. 2** Flow structure model for supersonic jet over a body of revolution.

where  $e_0 = C_v T + \frac{1}{2} u_i u_i + \frac{1}{2} \bar{u}'_i \bar{u}'_i$  and  $p = \rho R T$ .  $u_i$  and  $u'_i$  are the Cartesian components of the mean and fluctuating velocity, respectively.  $\rho$  is the static pressure;  $g_i$  is gravitational acceleration.  $\rho$  and  $\mu$  are density and viscosity, respectively.  $C_v$  and  $T$  are specific heat at constant volume and static temperature, respectively.  $R$  is the gas constant;  $q$  is the heat flux.

The Reynolds stress is modeled by the Boussinesq hypothesis as

$$\begin{aligned}\tau_{ij} &= -\rho \bar{u}'_i \bar{u}'_j = \mu_t \left( \frac{\partial u_i}{\partial x_j} + \frac{\partial u_j}{\partial x_i} \right) - \frac{2}{3} \left( \rho k + \mu_t \frac{\partial u_i}{\partial x_i} \right) \delta_{ij} \\ &= \mu_t S^2 / \frac{\partial u_j}{\partial x_i}\end{aligned}\quad (4)$$

The turbulent viscosity,  $\mu_t$ , is obtained via the shear-stress transport (SST)  $k-\omega$  turbulence model [18], whose accuracy and reliability has been widely demonstrated. Equation (5) shows the formula used to obtain the turbulent viscosity. The turbulent kinetic energy ( $k$ ) and specific dissipation rate ( $\omega$ ) are obtained by Eqs. (6) and (7), respectively.

$$\mu_t = \frac{\rho k}{\omega} \frac{1}{\max[\frac{1}{\alpha^*}, \frac{SF_2}{\alpha_1 \omega}]}\quad (5)$$

$$\begin{aligned}\frac{\partial}{\partial x_i} (\rho k u_i) &= \frac{\partial}{\partial x_i} \left( (\mu + \mu_t \sigma_k) \frac{\partial k}{\partial x_j} \right) \\ &+ \min(\mu_t S^2, 10 \rho \beta^* k \omega) - \beta^* \rho k \omega\end{aligned}\quad (6)$$

$$\begin{aligned}\frac{\partial}{\partial x_i} (\rho \omega u_i) &= \frac{\partial}{\partial x_i} \left( (\mu + \mu_t \sigma_\omega) \frac{\partial \omega}{\partial x_j} \right) + \rho \alpha S^2 - \beta \rho \omega^2 \\ &+ \frac{2}{\sigma_{\omega,2}} (1 - F_1) \rho \frac{1}{\omega} \frac{\partial k}{\partial x_i} \frac{\partial \omega}{\partial x_i}\end{aligned}\quad (7)$$

The coefficient,  $\alpha^*$ , damps the turbulent viscosity causing a low Reynolds number correction ( $\alpha^* = \frac{0.144\mu\omega + \rho k}{6\mu\omega + \rho k}$ ) and  $\alpha_1 = 0.31$ . Other closure coefficients are calculated as follows:

$$F_1 = \tanh \left( \min \left[ \max \left( \frac{\sqrt{k}}{0.09\omega y}, \frac{500\mu}{\rho y^2 \omega} \right), \frac{4\sigma_{\omega,2}\rho k}{D_\omega^+ y^2} \right] \right)^4\quad (8)$$

$$D_\omega^+ = \max \left[ 2\rho \frac{\sigma_{\omega,2}}{\omega} \frac{\partial k}{\partial x_j} \frac{\partial \omega}{\partial x_j}, 10^{-10} \right]\quad (9)$$

$$F_2 = \tanh \left( \max \left( \frac{2\sqrt{k}}{0.09\omega y}, \frac{500\mu}{\rho y^2 \omega} \right) \right)^2\quad (10)$$

$$\beta^* = 0.09 \left[ \frac{\frac{4}{15} + \left( \frac{\rho k}{8\mu\omega} \right)^4}{1 + \left( \frac{\rho k}{8\mu\omega} \right)^4} \right]\quad (11)$$

and

$$\alpha = \alpha_\infty \frac{(2.95\mu\omega + 9\rho k)(6\mu\omega + \rho k)}{9(2.95 + \rho k)(0.144\mu\omega + \rho k)}\quad (12)$$

where  $y$  is the distance to the next surface. The coefficients of  $\sigma_k$ ,  $\sigma_\omega$ ,  $\beta$ , and  $\alpha_\infty$  can be represented as  $\Phi$ , which satisfies Eq. (13).

$$\phi = F_1 \phi_1 + (1 - F_1) \phi_2\quad (13)$$

Here  $\sigma_{k,1} = 0.8603$ ,  $\sigma_{k,2} = 1$ ,  $\sigma_{\omega,1} = 0.5$ ,  $\sigma_{\omega,2} = 0.8562$ ,  $\beta_1 = 0.075$ ,  $\beta_2 = 0.0828$ ,  $\alpha_{\infty,1} = 0.5532$ , and  $\alpha_{\infty,2} = 0.4403$ .

To facilitate the validation of the numerical method, the jet in crossflow over an ogive cylinder studied by Brandeis and Gill [3] is selected as a benchmark case, as their measurements of force and

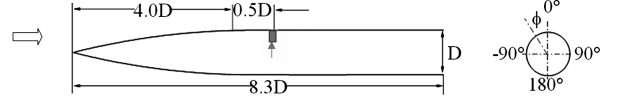


Fig. 3 Ogive cylinder configuration.

momentum as well as the detailed pressure distributions have been provided. Figure 3 shows the geometry of the ogive cylinder simulated in this study. The reference diameter ( $D$ ) of this model is 50 mm. A single circular nozzle with diameter ( $d$ ) of 8 mm is located 0.5D downstream of the ogive-cylinder junction with sonic flow at exit. The jet and flow conditions are identical to those of the experimental study by Brandeis and Gill [3] and are tabulated in Table 1.

The dimensions of the computational domain are tabulated in Table 2. For ease of specifying the jet conditions, a straight nozzle of 25 mm (0.5D) in length, which resided underneath the jet exit orifice, is included in the simulations. Only one half of the flow domain is modeled due to geometrical symmetry to reduce computational costs. To capture the shocks and vortices accurately, fine grids are built near the jet exit region and the body surfaces, whereas coarser grids are used in the far field region to improve the computational efficiency. Examples of meshes built for studying the circular nozzle by using Gambit™ are shown in Fig. 4. There are 11 patches in total.

The boundary types and conditions are specified in Table 3. Detailed values of physical quantities are provided in Table 1. A user-defined function program is compiled to extrapolate all the flow quantities at the outlet boundary from the plane adjoining the outlet plane.

The implicit, density-based finite-volume flow solver of FLUENT™ is used in this study to solve the RANS equations coupled with the SST turbulence model. The second-order upwind scheme is used for discretization. The global mass conservation is satisfied by reducing the residuals by at least 3 orders of magnitude.

The sensitivity of predicted pressure coefficient distributions to three sets of grids is shown in Figs. 5a and 5b. The coarse grid has 1,443,318 cells, while the medium and fine grids have 1,828,009 and 2,212,700 cells, respectively. The differences between solutions for the coarse and medium grids are observable in Fig. 5a, whereas further grid refinement does not produce much difference in the solutions. The grid convergence index (GCI) proposed by Roache [19,20] is calculated as a gauge of the grid refinement studies. The GCI in terms of relative error is given by Eq. (14).

$$GCI^{\text{fine}} = f_s |\varepsilon| / (r^n - 1)\quad (14)$$

Table 1 Freestream and jet conditions

	Jet ( $j$ )	Freestream ( $\infty$ )
Gas	Air, idea gas	Air, idea gas
Mach number ( $M$ )	1.0	3.3
Static pressure ( $P$ )	2944048 Pa	19029.89 Pa
Total pressure ( $P_t$ )	5572875 Pa	108867 Pa
Static Temperature ( $T$ )	366.34 K	84.2 K
Pressure ratio ( $PR = P_{j,t}/P_\infty$ )	292.8	
Momentum ratio ( $P_{j,t} M_j^2 / P_\infty \gamma_\infty M_\infty^2$ )	14.2	
Jet mass flow rate	0.54 kg/s	
Jet thrust	-177.6 N	

Table 2 Dimensions of computational domain

Parameter	Dimensions
Computational domain	Streamwise length, $\Delta x$
	Height, $\Delta y$
	Width, $\Delta z$
Diameter of cylinder ( $D$ )	50 mm

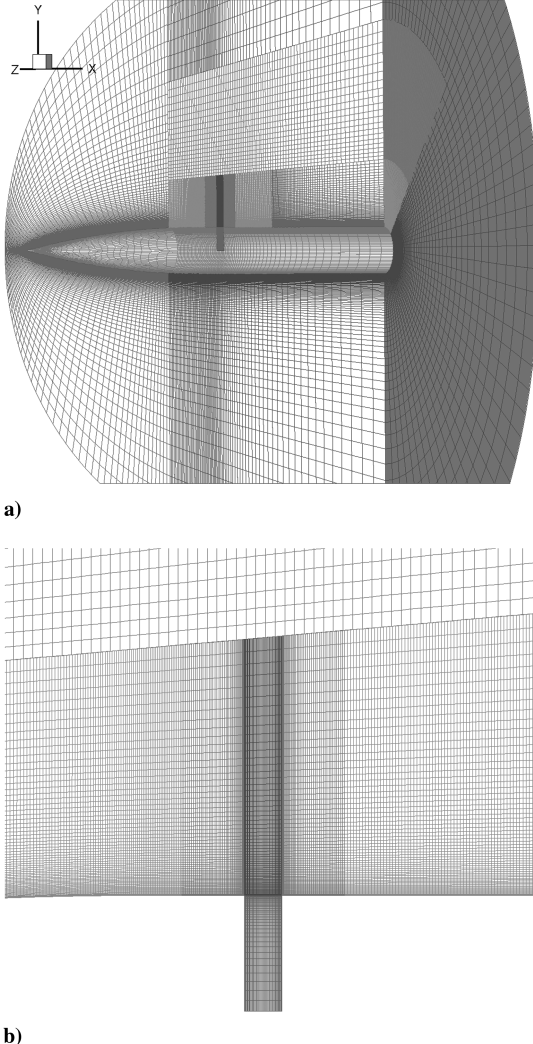


Fig. 4 Meshes built for simulation of lateral jet crossflow: a) three-dimensional view and b) side view of enlarged regions near the jet.

where  $n$  is the order of the numerical method; error  $\varepsilon = (f_2 - f_1)/f_1$ ,  $f_1$  and  $f_2$  are the solutions for fine and coarse grids, respectively. The grid refinement ratio  $r = (N_1/N_2)^{1/3}$ ,  $N_1$  and  $N_2$  are the number of elements on fine and coarse grids, respectively. The safety factor,  $f_s$ , is chosen as 3 as recommended by Roache [19,20] for normal applications. Thus, when a solution is within the asymptotic range, the GCI could be used as a worst-case estimation of the solution error to the given problem.  $GCI_{12}$  and  $GCI_{23}$  represent the grid convergence indices calculated from medium to coarse grids and fine to medium grids, respectively. Except the region near  $x/D = 7.5$ , both  $GCI_{12}$  and  $GCI_{23}$  have the same order of magnitude, suggesting near asymptotic behavior of the solution with increasing refinement of the grid. In addition, the maximum value of  $GCI_{23}$  is already less than 0.264. This is within the acceptance range for engineering calculations. Therefore, the medium grid is believed to provide sufficient accuracy. The comparison of the experimental and

Table 3 Boundary conditions

Boundary Types	Conditions
Outer radial boundaries	Freestream pressure, Mach number and temperature
Wall	No-slip, adiabatic
Jet inlet	Mass flow rate and temperature, $Ma = 1$
Downstream of outflow boundary	Extrapolate from interior points with zero gradient

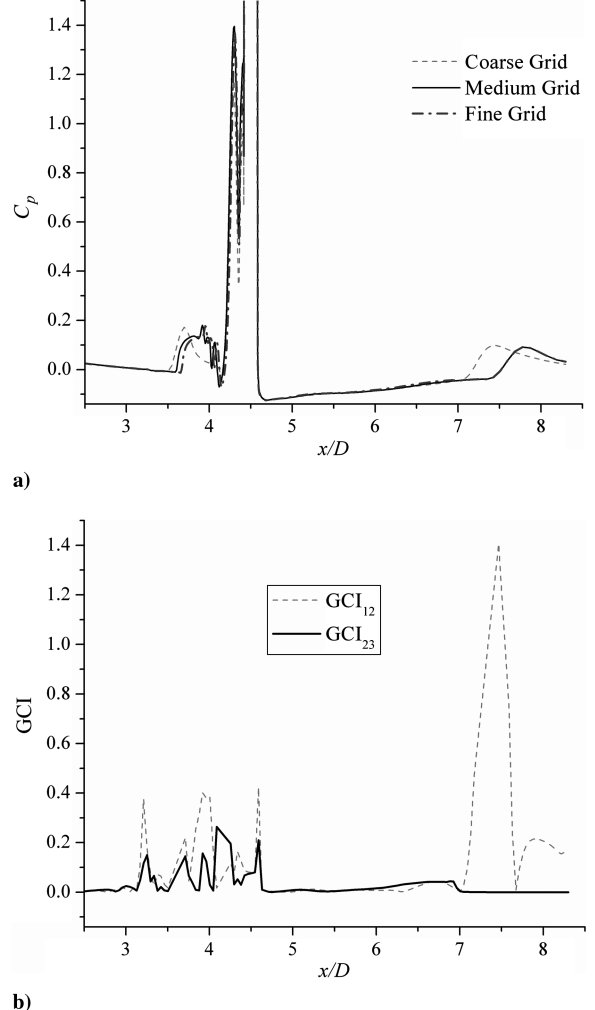


Fig. 5 Effect of grid refinement on a) longitudinal pressure coefficient ( $C_p$ ) distributions and b) GCI.

numerical results further credits the validity of current numerical simulation as described in section III.A.

The same numerical methods and grid generation techniques are used for investigating various nozzle shapes, and all the jet nozzles reside at the same location ( $x = 4.5D$ ). A complete simulation takes approximately 416 central processing unit hours by running in parallel using 16 processors.

## B. Jet Nozzle Shapes

Four nozzle shapes are considered in this study to investigate the effects of nozzle shape on the jet in supersonic crossflow over a body of revolution. For fair comparison, all jet nozzles have equivalent cross-sectional area as shown in Fig. 6. Case 1 is the baseline nozzle with a circular shape of diameter ( $d$ ) 8 mm, and the dimensions of the other three nozzle shapes are nondimensionalized with respect to  $d$ . Case 2 is an elliptical nozzle with minor semi-axis of  $l/d = 0.25$  and major semi-axis  $e/d = 1.0$ . Case 3 is a dropletlike-shaped nozzle with a cross section consisting of a tangentially mated semicircular arc and a half ellipse. The half ellipse has a major semi-axis of  $l/d = 0.375$  and a minor semi-axis of  $e/d = 0.370$ . The center of the circular arc is located vertically below the center of elliptic curve with a distance of  $5.43748d$ . The radius of the circular is  $5.80748d$ . From the junction point, the circular curve rotates clockwise of  $18.5127^\circ$  to reach the meridian line of the nozzle. Thus, the length of the nozzle ( $L/d$ ) is 1.48. Case 4 has the same geometry as case 3 but with the circular arc facing upstream. The critical geometrical parameters of these jet nozzle shapes are tabulated in Table 4.

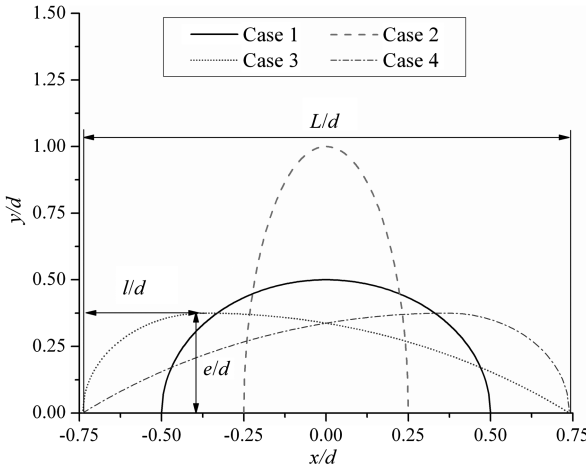


Fig. 6 Jet exit shapes for four cases.

### C. Interpretation of Force Decomposition and Amplification

In view of the interaction between the jet and external flow, two elements of the control force need to be considered [3]. The first comes directly from the jet thrust and the other from the complex interaction between the jet and the freestream. This jet freestream interaction is closely related to the flow structures and, thus, the surface of the cylindrical body can be divided into four distinct regions according to their flow characteristics. One is the flow separation region ahead of the jet orifice, which is generally associated with high pressure and causes a negative pressure force (as defined in Fig. 2), leading to an increase in the lateral control force. The other important region is the low-pressure region aft of the jet orifice due to the jet expansion, which leads to a positive pressure force. This region is normally followed by a recompression shock region due to pressure recovery. On the windward side of the wall, the flow is modified by the wraparound effect of the jet bow shock to form another high-pressure region. In terms of normal force, the downstream low-pressure and wraparound regions possess a surface pressure force opposite in direction to that of the jet thrust and results in an attenuation of the total normal force. However, the other two regions have surface pressure forces in the same direction as that of the jet thrust, thus augmenting the total normal force. Therefore, the normal force can be decomposed into various components, namely 1) jet thrust  $F_j$ , 2) pressure force ( $F_s$ ) in the flow separation zone ahead of the jet nozzle and a small region on the windward side of the wall having a negative surface pressure force, 3) pressure force ( $F_v$ ) in the downstream low-pressure region aft of the jet nozzle, 4) pressure force ( $F_w$ ) due to the jet bow shock wraparound effect on the windward side of the wall, and 5) pressure force ( $F_r$ ) due to shock recovery (further downstream). Note that items two through five contribute to the jet-interaction force  $F_{ij}$ . Figure 7 shows a typical diagram of the force decomposition.

To evaluate the effect of the force amplification and the deamplification due to the flow interaction, the force amplification factor ( $K$ ) is usually used, which is defined as the sum of the interaction force ( $F_{ij}$ ) and jet thrust ( $F_j$ ) normalized by the jet thrust [2,21],  $K = (F_j + F_{ij})/F_j$ . A larger  $K$  value is indicative of higher

lateral control efficiency. If  $K$  is less than 1, the jet interaction on the flowfield is unfavorable; in other words, the net normal force is less than the jet reaction force itself. Table 5 presents a breakdown of the various forces for different nozzle shapes. Both dimensional and nondimensional quantities are listed and clearly differentiate the force contributions from different flow regions. A more detailed discussion will be presented in the following sections.

## III. Results

### A. Validation of Numerical Results for Circular Nozzle

In the study of Brandeis and Gill [3], experiments were divided into two parts. In the first part, forces and momenta were measured by using a specially designed sting and force balance. In the second part, surface pressure distributions are measured by using static pressure taps.

For ease of validation, the pressure coefficients ( $C_p$ ) along the meridian line containing the baseline nozzle are shown in Fig. 8 together with those reported from experimental investigations [3]. Within the region of  $x/D \leq 3.6$  (labeled as "1" in figure), the  $C_p$  distribution is almost identical to the case without the lateral jet, viz. it decreases as the body slope decreases. The abrupt pressure variations within the region of  $3.6 \leq x/D \leq 4.3$  (labeled as "2") coincide with the clockwise rotating horseshoe vortex and its tertiary vortices presented in Fig. 9b due to the interaction between the jet and freestream. After the stagnation point at  $x/D = 4.3$ , an anticlockwise rotating vortex is formed in the region of  $4.3 \leq x/D \leq 4.42$  (labeled as "3"), where the pressure changes dramatically. It is found that the current numerical simulation accurately captures the features of the separation region.

Downstream of the jet orifice at  $x/D = 4.7$ , the pressure decreases acutely due to the vacuumlike region, which is caused by the jet expansion. The pressure then increases slightly, recovering to the freestream pressure up to  $x/D = 7.4$ , where the reflected shock reaches the wall as shown in Fig. 8. Beyond that, the pressure increases markedly due to the reflection shock. It is worth noting that within the region of  $4.6 \leq x/D \leq 7.4$ , the surface pressure is negative, resulting in an unfavorable force opposite to that of the jet reaction thrust. A detailed analysis of the flow structures will be provided in section III.B.

In addition to the pressure distribution, the normal force on the body is also calculated and compared. As shown in Table 5, the current simulation reports a normal force coefficient ( $C_n$ ) of  $-1.13$  for the circular nozzle, identical to the experimental study ( $-1.13$ ). The predicted momentum coefficient ( $C_m$ ) is  $-0.0622$  when momentum is referred to the center of the jet exit. This is less than the measured value of  $-0.09$  from the wind tunnel experiment. Note that the location of the reflection shock predicted by the simulation is almost 1 diameter downstream of the experimental location (as shown in Fig. 8), which could explain the disagreement on the pitching momentum. The other numerical study by Graham and Weinacht [10] also reports the similar difference of the reflection shock location as that of this study. These imply that the discrepancy of the reflection shock location predicted by computations and experiments could be attributable to the sting used in the wind tunnel experiments. It provides structural support to the ogive cylinder during the experiments and has a smaller diameter than the cylinder. The abrupt change of diameters at the end of the cylinder body may interfere with the flow, resulting in the upstream movement of the reflection shock in the experiments. From the preceding discussion, it can be seen that the results of the current simulation have very good agreement with the experiments.

### B. Jet Crossflow Interaction Over a Body of Revolution with a Circular Nozzle

#### 1. Flow Structures

In this section, the flow structures of the supersonic crossflow interaction over a body of revolution with a circular nozzle will be presented in detail. The work performed recently by Lu and Dickman [7], Viti et al. [8], and Dickman and Lu [9] are used for comparison, as

Table 4 Geometry parameters for various jet nozzle shapes ( $e/d$ ,  $l/d$ , and  $L/d$  are normalized by the reference diameter of circular nozzle,  $d = 8$  mm)

Case no	Shapes	$e/d$	$l/d$	$L/d$
1		0.500	0.500	1.000
2		1.000	0.250	0.500
3		0.370	0.375	1.480
4		Having the same parameters as those of case 3, with opposite orientation		

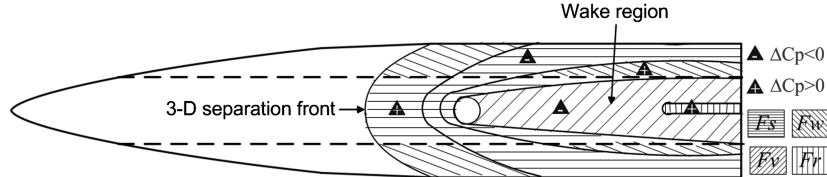


Fig. 7 Diagram of force decomposition.

detailed analyses on jet-interaction structures over a flat plate are provided in their studies.

Figure 9a shows the Mach number contours on the symmetry plane for the jet freestream interaction over the body of revolution with a circular nozzle. Similar to the crossflow over a flat plate as shown in Fig. 1, the jet bow shock forms ahead of the orifice, which promotes flow separation. After leaving the orifice, the jet expands and then recompresses through barrel shocks before ending with a Mach disk to slow down the highly supersonic flow inside the plume. Slip lines after the Mach disk and a triple point formed where the Mach disk intersects the barrel shock are also observable [8]. A reflected shock extends downstream from the triple point and impinges on the surface of the cylindrical body at  $x/D = 7.4$ . However, unlike the case of the flat plate, a body bow shock is present at the tip of the cylinder. Wrapped flow under the body is also observed, and a weak inclined shock is formed ahead of the wrapped flow due to thickening of the boundary layer.

More detailed flow structures ahead of the jet nozzle are shown in Fig. 9b with an enlarged view of Mach number contours and imprinted streamlines. Ahead of the jet, there is a complicated flow interaction region along the jet bow shock, barrel shock, and separation shock. Within close proximity to the separation shock and jet bow shock, the freestream velocity reduces significantly after passing through the separation shock and collides with the injected flow to form a saddle point. Subsequently, part of the air from freestream proceeds vertically upward, whereas some recedes from the saddle point accelerate towards the wall. Near the wall, a normal shock is formed to moderate the large differential flow velocity due to the presence of the wall. After passing through this normal shock, a flow stagnation point is found on the wall at about  $x/D = 4.3$ . Between the separation shock and the stagnation point, the flow separation region is dominated by a clockwise rotating vortex and an associated pair of tertiary vortices, which are believed to be the origin of the horseshoe vortex. Between the stagnation point and the barrel shock, an anticlockwise rotating vortex is observed. It can be seen that the flow structures ahead of the jet orifice are basically the same as those observed by Viti et al. [8] and Dickman and Lu [9] for the case of jet interaction on a flat plate. However, the tertiary vortices are not found in the study of Viti et al. [8]. They postulated that these tertiary vortices are a unique feature of the 2-D jet-interaction flowfield. Our results suggest that these tertiary vortices can also be observed in a three-dimensional (3-D) flow. For the anticlockwise rotating vortex, the studies of Dickman and Lu [9] revealed the existence of this vortex over the flat plate. However, they did not observe this vortex over a body of revolution, and they explained that the jet bow shock for the case of a body of revolution is refracted less than the case of a flat plane because the freestream Mach number in the flowfield downstream of the nose body shock is reduced. In fact,

they used a freestream Mach number of 2 as compared with 3.3 for our study. To verify whether the discrepancy observed could be due to the differences in freestream and jet conditions, we performed another numerical simulation with the freestream Mach number of 2 and other conditions the same as those of  $M = 3.3$ . The corresponding Mach number contours on the symmetry plane are shown in Fig. 10. In contrast to the case with Mach number of 3.3, the boundary layer thickness becomes thicker, and the stagnation point at the wall moves slightly upstream to about  $x/D = 4.2$ . The jet bow shock is also moved further upstream to about  $x/D = 3.9$  and is less refracted (including the barrel shock). It appears that the vortical structures just in front of the jet are more compressed (i.e., much smaller) and are lifted from the surface for the  $M = 2$  case. After adding sufficient streamlines, the anticlockwise rotating vortex is also captured for the case of  $M = 2$  in this study. It is worth noting that the rest of flow structures at  $M = 2$  are very similar to those of Dickmann and Lu [9]. Although these two cases have the same freestream Mach number of 2, their pressure ratio is different (PR = 292.8 for the current study and 2000 for the study of Dickmann and Lu [9]). The jet momentum ratio in the case studied by Dickmann and Lu [9] is much higher than that of the current study. The vortical structures just front of the jet could be much smaller due to stronger compression and because they were lifted further from the surface in their study than those reported in this study. Therefore, the anticlockwise rotation vortex could be present for the case study of Dickmann and Lu [9], but it is too small to be captured by their insufficient streamline visualization.

For the downstream jet-interaction flowfield, an isometric view of the flow around the injector with streamlines highlighting the main vortical structures is shown in Fig. 11. As reported by Viti et al. [8], for a jet in crossflow over a flat plane, such a plot can provide valuable insight of the flow structures. Figure 11 shows the Mach number contours mapped on the plane of symmetry, the  $C_p$  contours on the surface of body, and the vorticity magnitude contours with velocity vectors on the cross plane downstream of the nozzle at  $x/D = 6.4$ . Unlike the flow over a flat plate, it can be seen that the separated flow ahead of the jet orifice spreads laterally and downwards to the bottom of the body with the streamlines indicating the path of the horseshoe vortices. This wrapping effect forms a high-pressure region below the body, contributing unfavorably to the total control force. Other vortical systems aft of the jet are rather convoluted, but to some extent they are similar to the case of the crossflow over a flat plate as described by Viti et al. [8].

Now, we examine the surface trailing vortices, which are highlighted by the streamlines. The freestream appears to move away from the jet orifice as the barrel shock expands around the nozzle and moves back to the central plane when the barrel shock detaches from the surface. Viti et al. [8] believed that this surface trailing vortex

Table 5 Comparison of normal force and momentum for different nozzle shapes

Case no.	Shapes	Force (N)									
		$F_s$	$F_w$	$F_v$	$F_r$	$F_{ij} = F_s + F_w + F_v + F_r$	$F_j$	$C_n$	$C_j$	$C_m$	$K$
1		-33.9	16.2	34.9	-1.07	16.2	-177.6	-1.13	-1.24	-0.0622	0.91
2		-43.5	19.4	31.4	-0.016	7.4		-1.19		-0.0514	0.96
3		-29.2	15.2	37.1	-0.76	22.4		-1.08		-0.0699	0.87
4		-25.1	11.9	30.6	-2.89	14.5		-1.14		-0.0585	0.92

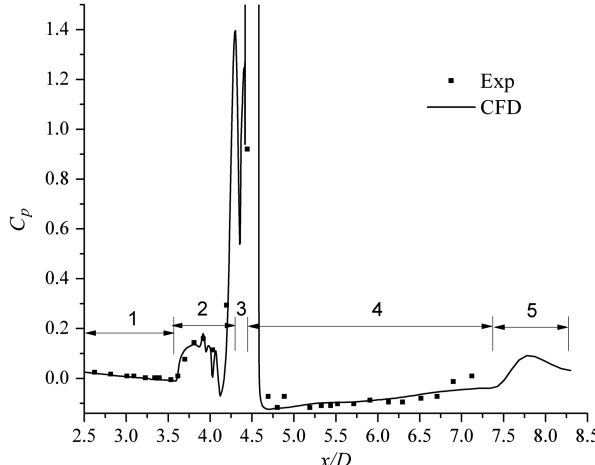


Fig. 8 Longitudinal pressure coefficient ( $C_p$ ) distributions for case 1.

originated from the second counter-rotating vortex ahead of the jet orifice, (referred to as the anticlockwise rotating vortex in this study as shown in Fig. 9b). In their studies, the left-running surface trailing vortex is observed as clockwise, and the right running vortex is anticlockwise. The same rotational sense of the surface trailing vortices is observed in this study as shown in Fig. 12. It appears that most of the fluid in the anticlockwise vortex departs from the surface (Fig. 11) forming the upper trailing vortex. Dickmann and Lu [9] revealed that the anticlockwise vortex over the flat plate convected

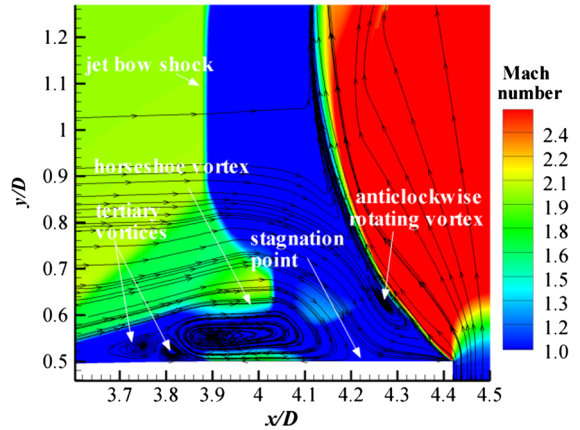
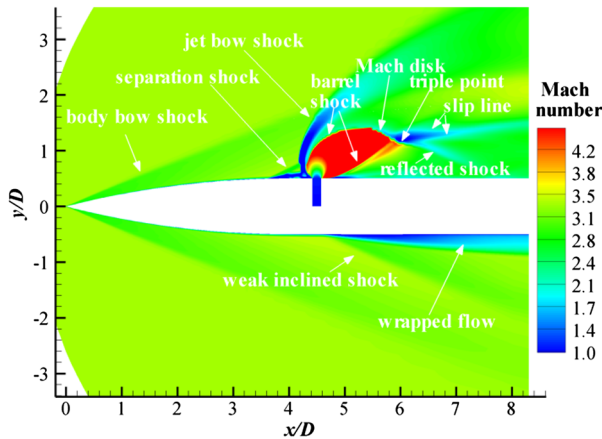
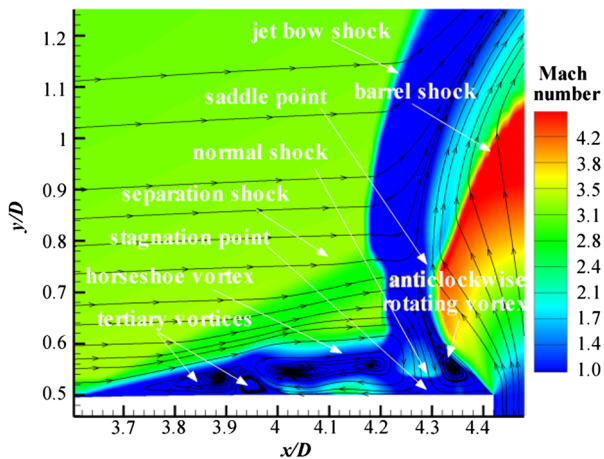


Fig. 10 Enlarged view of Mach number contours and imprinted streamlines on the symmetry plane upstream of case 1 at  $M = 2$ .



a)



b)

Fig. 9 Representative distributions of a) Mach number at symmetry plane and b) enlarged view of Mach number contours and imprinted streamlines on the symmetry plane upstream of case 1.

into the flow of the jet, rather than forming the downstream surface trailing vortex. They explained the existence of two sets of vortices downstream of the jet in terms of saddle points, a node of attachment and a node of separation using an oil surface-flow visualization technique combined with streamlines [7,9]. In this study, a similar technique is used as shown in Fig. 13. It shows the contours of pressure coefficient on the surface one grid distance from the cylindrical body with superimposed streamlines. It is worth noting that the oil flow picture is a 2-D representation of 3-D flow, so the out-of-plane velocity components are not observable. The separation and attachment lines located ahead of the jet orifice indicate the flow separation region, where the horseshoe vortex is generated and moves laterally. Downstream of the jet, the streamlines move along the separation lines until the saddle point where a set of surface trailing vortices are spawned (Fig. 12). This surface trailing vortex is generated due to the strong upwash effect, when the barrel shock detaches from the surface. Downstream of the barrel shock, the upwash flow and the injected fluid form a dominant right running vortex, which is clockwise (trailing vortices 3), accompanied by the a left-running anticlockwise trailing vortex as shown in Fig. 12. As the barrel shock detaches from the surface, a low-pressure region is formed. This low-pressure region allows the surface trailing vortex to

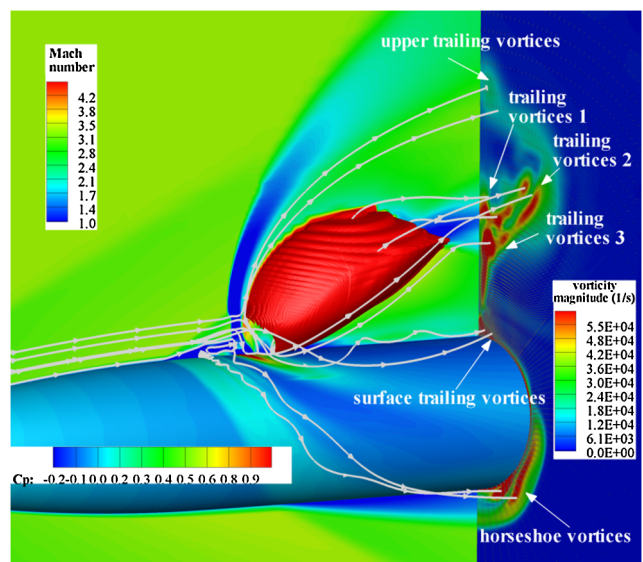


Fig. 11 Isometric view of flow around the injector with streamlines highlighting the main vortical structures of case 1. Mach number contours on symmetry plane,  $C_p$  contours on surface of wall, vorticity magnitude contours with velocity vectors (y-z projection) superimposed on cross plane of  $x/D = 6.4$ , and barrel shock represented by the Mach number of 4.4 isosurface.

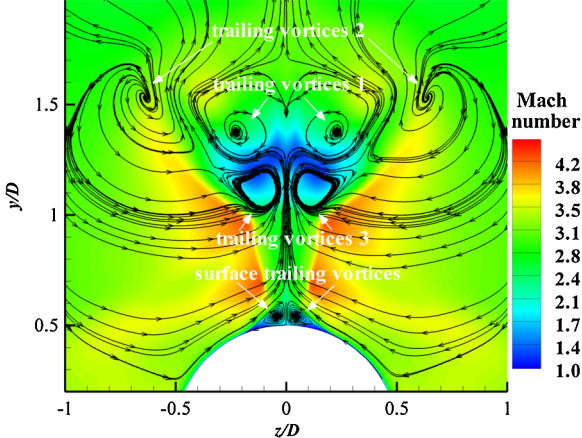


Fig. 12 Mach number contours and imprinted streamlines at  $x/D = 6.4$  of crossflow for circular nozzle. The flow is into the plane of the page.

reside at the center of the wall along the attachment line before reaching the recompression shock near the end of cylindrical body.

There are other trailing vortices as shown in Figs. 11 and 12. As discussed in the preceding paragraphs, the upper trailing vortex emanating from the anticlockwise vortex just ahead of the jet orifice follows the windward edge of barrel shock but is relatively much weaker, and this prevents it from being traced clearly. The trailing vortices 1 and 3 are two counter-rotating vortices formed near the Mach disk. Trailing vortex 2 is located just outside of the barrel shock shear layer region. Part of the fluid in trailing vortices 1, 2, and 3 comes from the incoming freestream, which moves towards the wall ahead of the jet orifice before being convected downstream by shearing the barrel shock. Amongst all these vortices, the surface trailing vortices are located close to the wall and have much more influence on the interaction force. The other trailing vortices play a larger role in the mixing mechanism.

## 2. Analysis of Force Components

Now, we examine the various force components with respect to the different flow regions as described in section II.C. The force decomposition data for the circular nozzle (case 1) is tabulated in the first row of Table 5. As can be found, the flow separation ( $F_s$ ), wrapping ( $F_w$ ), and vacuum ( $F_v$ ) regions have significant contributions to the total normal force. The detailed analysis of the flow structures is provided in section III.B.1. Related with the flow separation ahead of jet orifice is the horseshoe vortices and the high pressure, which results in the attendant force having the same direction as that of the jet thrust, thus augmenting the control force by almost 20% (the total jet reaction force is about 160 N). However, these horseshoe vortices shed laterally along the footprint of the jet

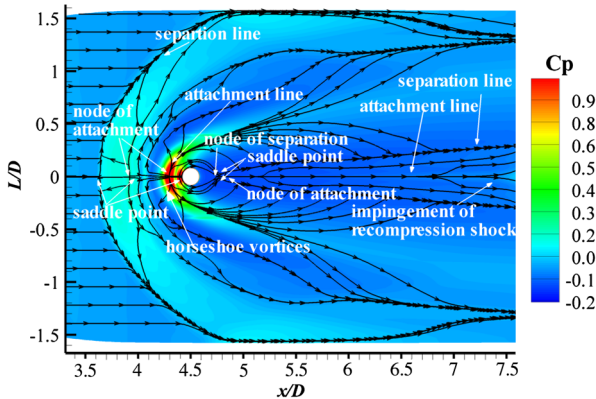


Fig. 13 Streamlines above the ogive cylinder simulating oil surface-flow visualization with superimposed contours of pressure coefficient of case 1.

bow shock and wrap the body of revolution. On the windward side of the wall, it produces the force ( $F_w$ ) having the opposite direction to that of the jet thrust, leading to reduction of the jet reaction force by about 10%. Downstream of the jet, the force ( $F_v$ ) also attenuates the jet reaction force by about 20%.

For the low-pressure region downstream of the jet orifice, the surface trailing vortices and the indent of the leeside barrel shock are reported to be the main contributors by Viti et al. [8] for the crossflow over a flat plate. The origin and evolution of the surface trailing vortices for the crossflow over an ogive cylinder are discussed in section III.B.1 of this study, whereas the detailed analysis of the leeside barrel shock on the cylinder body will be presented in the next section. As can be seen, the force decomposition clearly indicates the importance of the flow structures upstream and downstream of the jet orifice.

## C. Effects of Jet Nozzle Shape

Four nozzle shapes (cases 1–4) are examined in this study, and their dimensions are given in Table 4. They are, in the following order: the circular nozzle, elliptical nozzle, and two dropletlike-shaped nozzles of opposing orientation. The overall effects of nozzle shape on aerodynamic forces and their corresponding force components are presented in Table 5. It can be seen clearly that all nozzles produce unfavorable interaction forces ( $F_{ij}$ ). The elliptical nozzle produces the smallest interaction force, followed by the inverse dropletlike-shaped nozzle (case 4), circular nozzle (case 1), and dropletlike-shaped nozzle (case 3). As tabulated in Table 5, the elliptical nozzle has the largest force amplification factor of 0.96 compared with 0.91 of the baseline model, indicating that the elliptical nozzle is the most efficient nozzle shape.

Now, we focus on how the nozzle shape affects the flow separation ahead of the jet orifice and the low-pressure region aft of the jet orifice. Figure 14 shows the contours of pressure coefficients for these four nozzle shapes. For ease of comparison, the surface pressure distributions have been unwrapped. It can be seen that the high-pressure region ahead of the jet orifice due to the flow separation is the largest for the elliptical nozzle and the smallest for the inverse dropletlike-shaped nozzle (case 4). The elliptical nozzle also has the highest pressure values in this high-pressure region ahead of jet orifice among the four nozzle shapes, especially at  $4.1 \leq x/D \leq 4.3$ , as shown in Fig. 15. It follows that the nozzle with a wider length in the windward lateral direction can produce a larger surface area of the windward barrel shock as seen in Fig. 16. This promotes stronger and more extensive interaction between the freestream and jet, which leads to stronger flow separation ahead of the jet orifice. These results are consistent with those reported in Brandeis and Gill [3] in that the nozzle of the rectangular slit with the larger side facing the external flow produced larger upstream separation.

The effects of nozzle shape on downstream flow structures and pressure distributions are less straightforward. As shown in Fig. 15, the dropletlike-shaped nozzle (case 3) has the lowest pressure aft of the jet orifice along the meridian line (containing the nozzle). Therefore, it produces lower pressure (viz. larger interaction force  $F_v$ ) due to the flow vacuum region downstream of the jet orifice. Accordingly, a lower  $F_v$  (see Table 5) is produced by the elliptical nozzle and the inverse dropletlike-shaped nozzle (case 4) due to their high pressure in the flow vacuum region as shown in Fig. 15. It is promising that the elliptical nozzle not only produces a larger favorable separation force upstream of the nozzle, but it also generates a relatively smaller unfavorable normal force downstream of the nozzle, leading to a higher force amplification factor of 0.96.

This difference in the downstream pressure distributions of different nozzle shapes may be attributed to the differences in the strength and topologies of the surface trailing vortices. As shown in Fig. 17, there is one pair of surface trailing vortices at  $x/D = 5.2$  for all the four nozzle shapes. But the regions influenced by these surface trailing vortices have different sizes. Among these four nozzle shapes, case 2 has the smallest surface trailing vortices in size. Each surface trailing vortex has a tertiary vortex downstream at the location of  $x/D = 5.5$  except for the inverse dropletlike-shaped

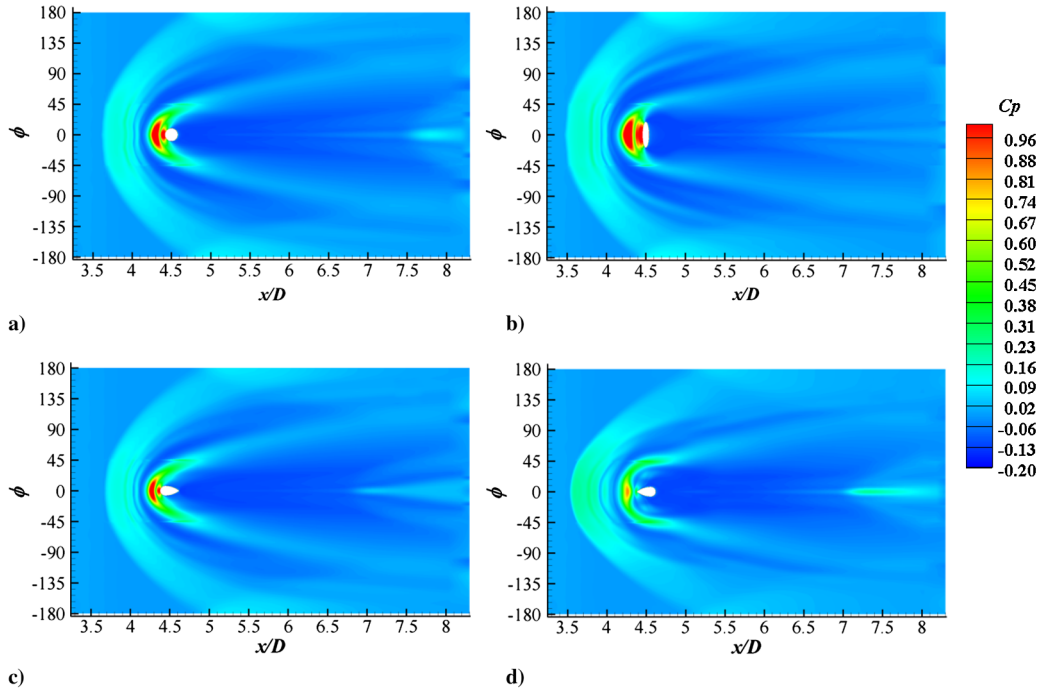


Fig. 14 Pressure coefficient ( $C_p$ ) distributions at the lateral walls of a) case 1, b) case 2, c) case 3, and d) case 4.

nozzle (case 4), in which each surface trailing vortex has two tertiary vortices. Therefore, the strength of the surface trailing vortices is reduced as they convect downstream (from  $x/D = 5.2$  to  $5.5$ ), especially for case 4. These smaller sized (case 2) or weaker strength (case 4) surface trailing vortices could lead to a lower unfavorable normal force, which is generated due to the flow vacuum region downstream of the jet orifice.

It is interesting to note that the leeward barrel shock generated by the dropletlike-shaped nozzle has a tail as shown in Fig. 16. This is unique among the four nozzle shapes. To better understand it, Fig. 18 shows a comparison of Mach number contours and  $C_p$  on the unwrapped surface with a distance of  $0.1D$  and  $0.00084D$  to the wall between case 1 and case 3. As seen in Fig. 18a, in this tail region, the Mach number is higher for the dropletlike-shaped nozzle than for the circular nozzle. It is suspected that the jet plume is shifted laterally before fully expanding. In the region very near to the wall, a sink is observed immediately downstream of the nozzle as seen in Fig. 18b. This represents a 3-D flow separation region immediately downstream of the dropletlike-shaped nozzle due to the sharp edge at the downstream tip. This small flow separation region inhibits the full expansion of the jet column in the leeward direction. Therefore, the Mach number increases in the tail region as shown in Fig. 18a.

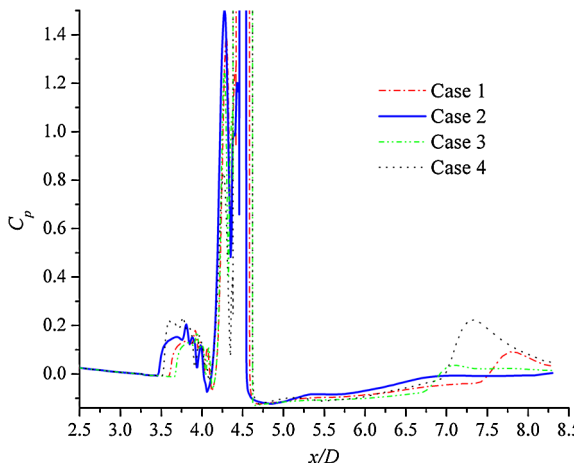


Fig. 15 Longitudinal pressure coefficient ( $C_p$ ) distributions of case 1, 2, 3, and 4.

Viti et al. [8] observed that the low-pressure region aft of the jet orifice is generated by the combined effects of the concave indent in the leeside of the barrel shock and the surface trailing vortices. The reflection of the barrel shock on the solid surface creates a concave indent in the leeward side of the barrel shock that promotes the lowering of the local pressure and constrains the surface trailing vortex as it attaches to the wall surface. In the same way, Fig. 19 shows a downstream view of the barrel shock represented by the Mach 4.4 isosurface and Mach number contours with velocity vectors at a cross plane of  $x/D = 5.0$  for four different nozzle shapes. In this figure, the concave indent, inflection line, and inner reflection line can be observed.

For the inverse dropletlike-shaped nozzle (case 4), its barrel shock has a similar structure as that of the circular nozzle, but the resulting barrel shock is located at a further distance from the wall. This means that there is more room to accommodate the surface trailing vortex, and the effect of the concave indent on the surface pressure is reduced. In addition, the angle of the inflection line to the midline increases gradually along the downstream direction. Therefore, the indent becomes flatter along the downstream direction compared with that of the circular nozzle. Thus, the pressure force due to the flow vacuum for case 4 is the minimum among all these cases as tabulated in Table 5.

For case 2 with the elliptical nozzle, two distinct features are found in Fig. 19. One is that the leeward barrel shock has the smallest lateral length as the jet spreads largest in its minor direction as seen in Fig. 16. One reason for this kind of jet spreading characteristic could

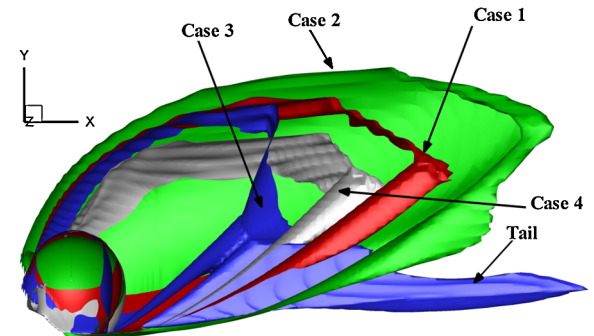


Fig. 16 Isometric view of the Mach 4.4 isosurface for four cases.

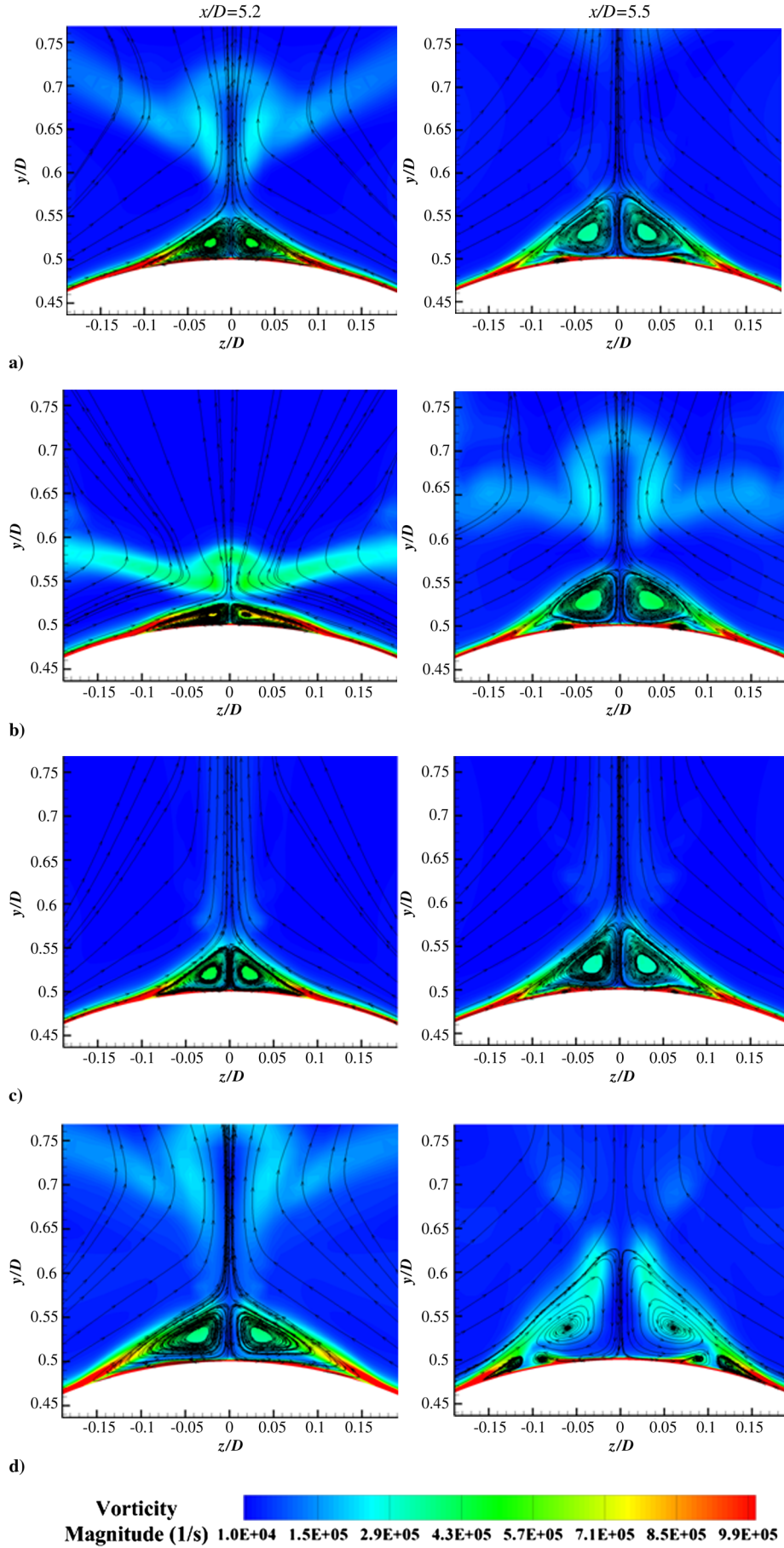


Fig. 17 Vorticity magnitude contours and imprinted streamlines at  $x/D = 5.2$  and  $5.5$  for a) case 1, b) case 2, c) case 3, and d) case 4.

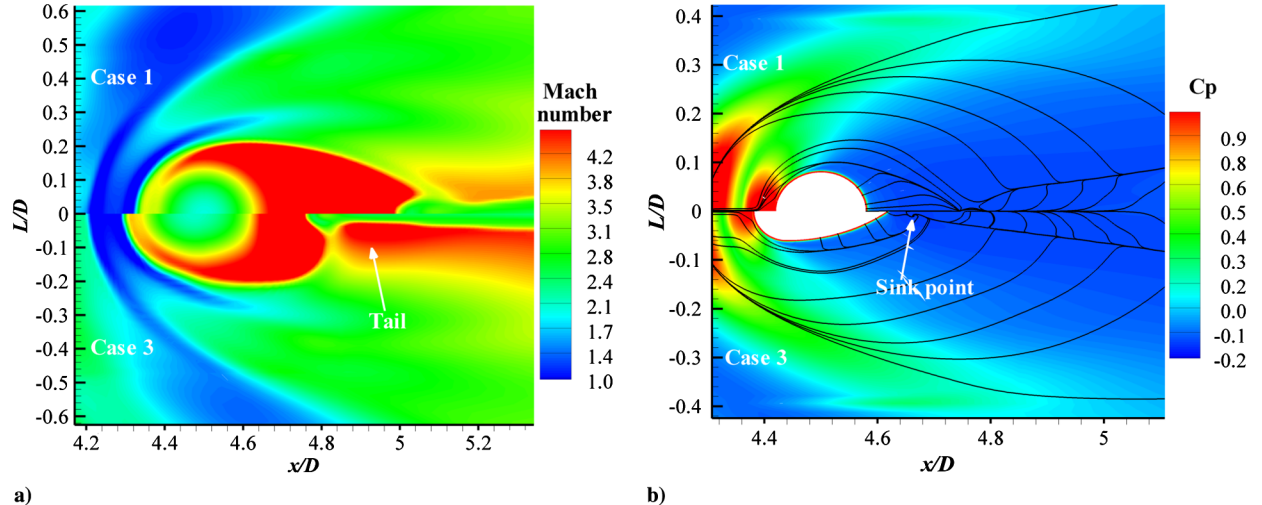


Fig. 18 Comparisons of case 1 and case 3 on a) Mach number distribution at the unwrapped surface with  $0.1D$  distance to the wall and b) imprinted streamlines with  $C_p$  distribution at the unwrapped surface with  $0.00084D$  distance to the wall.

be due to the axis-switching phenomenon for jet columns of elliptical nozzles [15,22,23]. This phenomenon is associated with an underexpanded jet injected from an elliptical sonic nozzle, which spreads rapidly in the minor axis direction and maintains an almost constant width or contracts in the major axis direction. This has been observed for subsonic elliptical jets [24]. The other reason could be due to the rapid folding of the barrel shock towards its inner side as it moves downstream. As seen in Fig. 19b, the inflection line of the barrel shock deviates towards the midline along the downstream direction. The barrel shock far away from the wall folds inside more rapidly than that near the surface.

The other feature is that no concave indent is observed in the vicinity downstream of the orifice. Thus, the surface trailing vortex only occupies a small region near the wall. These two features provide a

possible explanation as to why the elliptical nozzle produces a smaller low-pressure region compared with the circular nozzle.

For the dropletlike-shaped nozzle (case 3), the barrel shock has two tails in the left and right sides. A sharp indent is created due to the sharp end of the nozzle as the flow moves downstream. Therefore, the surface trailing vortex is confined to the near wall, and it promotes the lowest pressure force within the flow vacuum region as shown in Table 5.

As this study focuses on the first type of lateral control using a jet located at the center of gravity to induce parallel movement of the vehicle, minimizing the pitching momentum is preferred. The center of the jet exit is taken as the reference for calculating momentum. From Table 5, it can be found that all of these nozzles produce negative momentum, (i.e., the body pitches down). The elliptical

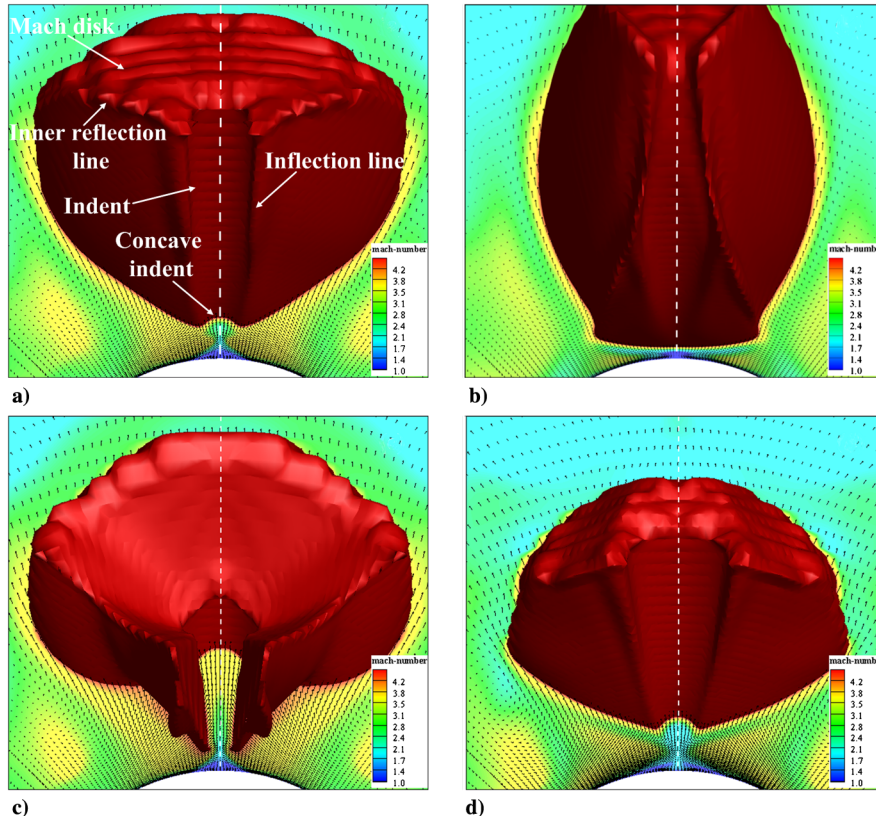


Fig. 19 Downstream view of the barrel shock represented by Mach 4.4 isosurface and Mach number contours with velocity vectors (y-z projections) at the cross plane of  $x/D = 5$  for a) case 1, b) case 2, c) case 3, and d) case 4. The flow is out of the plane of the page.

nozzle is the best among these four models in terms of reducing the pitching-down momentum, whereas the inverse dropletlike-shaped nozzle (case 4) performs better than the baseline by virtue of its lower momentum. In general, the elliptical nozzle shape is the best nozzle shape among these four models with respect to enhancing the normal force and reducing the pitching momentum.

Analysis of the pressure force components and structures of the barrel shock reveals that the flow separation region is closely related to the windward barrel shock. A larger windward facing barrel shock surface promotes the flow separation ahead of the jet orifice. As the horseshoe vortices in the flow separation region shed laterally downstream, they wrap around the surface and result in an unfavorable effect on the normal force. In addition, the vacuum region aft of the jet orifice is closely related to the surface trailing vortices and the leeward barrel shock topologies, such as its indent and inflection lines.

#### IV. Conclusion

This numerical study investigates the main flow structures arising from the interaction between a sonic jet and the supersonic external flow over a body of revolution via solving the Navier-Stokes equations. Several flow structures have been captured, such as the flow separation region ahead of the jet orifice, the vacuum region aft of the jet orifice, and the subsequent pressure recovery region.

Detailed analysis of flow structures and force components indicates that the flow separation and vacuum regions play important roles in the consequent interaction force. In the flow separation region, the horseshoe vortices are generated and shed laterally along the footprint of the jet bow shock, which tends to wrap around the body of revolution. This wrapping effect weakens the interaction force and has an unfavorable effect on the normal force, which is significantly different from the case of the crossflow over a flat plate, where the horseshoe vortices shed sideways along the cross-stream direction. Therefore, the influence of the separation region on the interaction force is reduced for the body of revolution compared with that of a jet in crossflow over a flat plate.

Downstream flow structures over the body of revolution are basically similar to those of the crossflow over a flat plate. The upper trailing vortex emanating from the anticlockwise vortex just ahead of the jet orifice follows the windward edge of barrel shock, and part of the anticlockwise vortex forms three trailing vortices. There are two counter-rotating vortices near the Mach disk and another trailing vortex is located just outside of the barrel shock shear layer region. Among all the vortices, the horseshoe and surface trailing vortices are located close to the wall and have significant influence on the interaction force. The rest of the trailing vortices form the main mechanisms of mixing.

Effects of jet nozzle shape on the jet crossflow interaction are further investigated and analyzed. These circular, elliptical, dropletlike-shaped, and inverse dropletlike-shaped nozzles have equivalent cross-sectional area. The results indicate that the elliptical nozzle with its semimajor axis in the crosswise orientation not only produces a larger favorable separation force upstream of the nozzle, but also generates a relatively smaller unfavorable normal force downstream of the nozzle, resulting in better performance.

Analysis of the pressure force components and structures of the barrel shock shows that the flow separation region is closely related to the windward barrel shock. The jet spreading promotes flow separation ahead of the jet orifice. As the horseshoe vortices in the flow separation region shed laterally downstream, they wrap around the surface causing a decrease in the interaction force. In addition, the vacuum region aft of the jet orifice is related to the surface trailing vortices and the leeward barrel shock topology, such as its indent and inflection lines. The elliptical nozzle produces a reduced low-pressure region compared with the circular nozzle for two reasons. Firstly, the width of the leeward barrel shock is smallest for the elliptical nozzle due to either axis-switching [22–24] or rapid folding inside of the barrel shock. The other is that no concave is observed downstream of the orifice. As such, the surface trailing vortex only occupies a small region near the wall.

#### References

- [1] Margason, R. J., "Fifty Years of Jet in Crossflow Research," AGARD CP-534, 1993, pp. 1-1-1-41.
- [2] Champigny, P., and Lacau, R. G., "Lateral Jet Control for Tactical Missiles," AGARD 804, 1994, pp. 3-1-3-57.
- [3] Brandeis, J., and Gill, J., "Experimental Investigation of Side-Jet Steering for Supersonic and Hypersonic Flow," *Journal of Spacecraft and Rockets*, Vol. 33, No. 3, 1996, pp. 346–352.  
doi:10.2514/3.26766
- [4] Mahmud, Z., and Bowersox, R. D. W., "Aerodynamics of Low-Blowing-Ratio Fuselage Injection into a Supersonic Freestream," *Journal of Spacecraft and Rockets*, Vol. 42, No. 1, 2005, pp. 30–37.  
doi:10.2514/1.4803
- [5] Morkovin, M. V., Migotsky, E., Bailey, H. E., and Phinney, R. E., "Experiments on Interaction of Shock Waves and Cylindrical Bodies at Supersonic Speeds," *Journal of the Aeronautical Sciences*, Vol. 19, No. 4, 1952, pp. 237–248.
- [6] Chenault, C. F., Beran, P. S., and Bowersox, R. D. W., "Numerical Investigation of Supersonic Injection Using a Reynolds-Stress Turbulence Model," *AIAA Journal*, Vol. 37, No. 10, 1999, pp. 1257–1269.  
doi:10.2514/2.594
- [7] Lu, F. K., and Dickmann, D. A., "Topology of Supersonic Jet Interaction Flowfields at High Pressure Ratios," *13th International Symposium on Flow Visualization*, Universite De Franche Comte Paper 235, Nice, France, 2008.
- [8] Viti, V., Neel, R., and Schetz, J. A., "Detailed Flow Physics of the Supersonic Jet Interaction Flowfield," *Physics of Fluids*, Vol. 21, No. 4, 2009, 046101.  
doi:10.1063/1.3112736
- [9] Dickmann, D. A., and Lu, F. K., "Shock/Boundary Layer Interaction Effects of Transverse Jets in Crossflow Over a Body of Revolution," *19th AIAA Computational Fluid Dynamics*, AIAA Paper 2009-4146, San Antonio, TX, 2009.
- [10] Graham, M. J., and Weinacht, P., "Numerical Investigation of Supersonic Jet Interaction for Axisymmetric Bodies," *Journal of Spacecraft and Rockets*, Vol. 37, No. 5, 2000, pp. 675–683.  
doi:10.2514/2.3617
- [11] Spaid, F. W., "Two-Dimensional Jet Interaction Studies at Large Values of Reynolds Numbers," *AIAA Journal*, Vol. 13, No. 11, 1975, pp. 1430–1434.  
doi:10.2514/3.7011
- [12] Haven, B. A., and Kurosaka, M., "Kidney and Anti-Kidney Vortices in Crossflow Jets," *Journal of Fluid Mechanics*, Vol. 352, 1997, pp. 27–64.  
doi:10.1017/S0022112097007271
- [13] Weston, R. P., and Thames, F. C., "Properties of Aspect-Ratio-4.0 Rectangular Jets in a Subsonic Crossflow," *Journal of Aircraft*, Vol. 16, No. 10, 1979, pp. 701–707.  
doi:10.2514/3.58592
- [14] Barber, M. J., Schetz, J. A., and Roe, L. A., "Normal Sonic Helium Injection Through a Wedge-Shaped Orifice into Supersonic Flow," *Journal of Propulsion and Power*, Vol. 13, No. 2, 1997, pp. 257–263.  
doi:10.2514/2.5157
- [15] Gruber, M. R., Nejad, A. S., Chen, T. H., and Dutton, J. C., "Transverse Injection From Circular and Elliptic Nozzles into a Supersonic Crossflow," *Journal of Propulsion and Power*, Vol. 16, No. 3, 2000, pp. 449–457.  
doi:10.2514/2.5609
- [16] Srinivasan, R. W., and Bowersox, R. D., "Transverse Injection Through Diamond and Circular Ports into a Mach 5.0 Freestream," *AIAA Journal*, Vol. 46, No. 8, 2008, pp. 1944–1962.  
doi:10.2514/1.29253
- [17] Viti, V., Wallis, S., Schetz, J. A., Neel, R., and Bowersox, R. D. W., "Jet Interaction with a Primary Jet and an Array of Smaller Jets," *AIAA Journal*, Vol. 42, No. 7, 2004, pp. 1358–1368.  
doi:10.2514/1.4850
- [18] Menter, F. R., "Two-Equation Eddy-Viscosity Turbulence Models for Engineering Applications," *AIAA Journal*, Vol. 32, No. 8, 1994, pp. 1598–1605.  
doi:10.2514/3.12149
- [19] Roache, P. J., "Perspective: a Method for Uniform Reporting of Grid Refinement Studies," *Journal of Fluids Engineering*, Vol. 116, No. 3, 1994, pp. 405–413.  
doi:10.1115/1.2910291
- [20] Roache, P. J., "Verification of Codes and Calculations," *AIAA Journal*, Vol. 36, No. 5, 1998, pp. 696–702.  
doi:10.2514/2.457

- [21] Seiler, F., Gnemmi, P., Ende, H., Schwenzer, M., and Meuer, R., "Jet Interaction at Supersonic Cross Flow Conditions," *Shock Waves*, Vol. 13, No. 1, 2003, pp. 13–23.  
doi:10.1007/s00193-003-0189-y
- [22] Hussain, F., and Husain, H. S., "Elliptic Jets. Part 1. Characteristics of Unexcited and Excited Jets," *Journal of Fluid Mechanics*, Vol. 208, 1989, pp. 257–320.  
doi:10.1017/S0022112089002843
- [23] Miller, R. S., Madnia, C. K., and Givi, P., "Numerical Simulation of Noncircular jets," *Computers and Fluids*, Vol. 24, No. 1, 1995,  
pp. 1–25.  
doi:10.1016/0045-7930(94)00019-U
- [24] Schadow, K. C., Gutmark, E., Koshigoe, S., and Wilson, K. J., "Combustion-Related Shear-Flow Dynamics in Elliptic Supersonic Jets," *AIAA Journal*, Vol. 27, No. 10, 1989, pp. 1347–1353.  
doi:10.2514/3.10270

J. Oefelein  
*Associate Editor*